

See discussions, stats, and author profiles for this publication at: <https://www.researchgate.net/publication/277410873>

Understanding the Origin of Enhanced Performances in Core–Shell and Concentration–Gradient Layered Oxide Cathode Materials

ARTICLE in ACS APPLIED MATERIALS & INTERFACES · MAY 2015

Impact Factor: 6.72 · DOI: 10.1021/acsaami.5b02373 · Source: PubMed

CITATION

1

READS

21

5 AUTHORS, INCLUDING:



Dawei Song

Nankai University

52 PUBLICATIONS 604 CITATIONS

[SEE PROFILE](#)



Lianqi Zhang

51 PUBLICATIONS 810 CITATIONS

[SEE PROFILE](#)

Understanding the Origin of Enhanced Performances in Core–Shell and Concentration-Gradient Layered Oxide Cathode Materials

Dawei Song,^{†,‡} Peiyu Hou,^{†,‡,§} Xiaoqing Wang,[‡] Xixi Shi,[†] and Lianqi Zhang^{*,†}

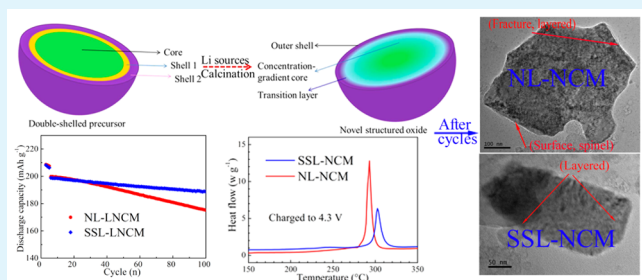
[†]Tianjin Key Laboratory for Photoelectric Materials and Devices, School of Materials Science and Engineering, Tianjin University of Technology, Tianjin 300384, China

[‡]School of Environment and Chemical Engineering, Tianjin Polytechnic University, Tianjin 300387, China

Supporting Information

ABSTRACT: Core–shell and concentration-gradient layered oxide cathode materials deliver superior electrochemical properties such as long cycle life and outstanding thermal stability. However, the origin of enhanced performance is not clear and seldom investigated until now. Here, a specific structured layered oxide ($\text{LiNi}_{0.5}\text{Co}_{0.2}\text{Mn}_{0.3}\text{O}_2$) consisting of concentration-gradient core, transition layer, and stable outer shell, is designed and achieved from double-shelled precursors to overcome the great challenge by comparison with the normal layered $\text{LiNi}_{0.5}\text{Co}_{0.2}\text{Mn}_{0.3}\text{O}_2$. As expected, the specific structured layered oxide displays excellent cycle life and thermal stability. After numerous cycles, the valence state of Ni and Co at normal layered oxide surface tends to a higher oxidation state than that of the specific structured oxide, and the spinel phase is observed on particle surface of normal layered oxide. Also, the deficient spinel/layered mixed phases lead to high surface film and charge-transfer resistance for normal layered oxide, whereas the specific structured one still remains a layered structure. Those results first illustrate the origin of improved electrochemical performance of layered core–shell and concentration-gradient cathode materials for lithium-ion batteries.

KEYWORDS: double-shelled precursors, specific structure, surface transition, cathode materials, lithium-ion batteries



1. INTRODUCTION

In the past decade, rechargeable lithium-ion batteries (LIBs) became the main power sources for electric devices since they were commercialized by Sony in 1991.^{1,2} Cathode materials play an increasingly important role in LIBs, and LiCoO_2 is widely used due to its large capacity and easy preparation. Recently, layered oxides $\text{LiNi}_{1-x,y}\text{Co}_x\text{Mn}_y\text{O}_2$ have the advantages of low cost, weak toxicity, and large specific capacity, while the commercialized LiCoO_2 displays some intrinsic drawbacks such as high cost and structural instability at high upper cutoff voltages.^{3–16} However, these layered materials are structurally unstable during thermal runaway reactions due to the oxygen release from the host structure, especially at high operating voltage over 4.4 V and temperature above 55 °C, resulting in inferior thermal properties at the highly charged state and poor cycle stability, which hinders its wide commercialization in a lithium battery system.^{17,18}

In recent years, the core–shell structure including one shell and double shells,^{19–22} and concentration-gradient structure^{23–25} have been adopted to solve the above problems for these layered materials. Sun's group and Argonne National Laboratory first report the microscale spherical core–shell structured $\text{Li}[(\text{Ni}_{0.8}\text{Co}_{0.1}\text{Mn}_{0.1})_{0.8}(\text{Ni}_{0.5}\text{Mn}_{0.5})_{0.2}]\text{O}_2$, in which core $\text{LiNi}_{0.8}\text{Co}_{0.1}\text{Mn}_{0.1}\text{O}_2$ and shell $\text{LiNi}_{0.5}\text{Mn}_{0.5}\text{O}_2$ provide large specific capacity and structural stability, respectively.¹⁹ Consequently, this core–shell layered oxide has a superior cycle life

and enhanced thermal stability compared to the core $\text{LiNi}_{0.8}\text{Co}_{0.1}\text{Mn}_{0.1}\text{O}_2$. It should be noted that there exists much compositional difference between the core–shelled $\text{Li}[(\text{Ni}_{0.8}\text{Co}_{0.1}\text{Mn}_{0.1})_{0.8}(\text{Ni}_{0.5}\text{Mn}_{0.5})_{0.2}]\text{O}_2$ and core $\text{LiNi}_{0.8}\text{Co}_{0.1}\text{Mn}_{0.1}\text{O}_2$. The improved performance coming from core–shell structure or change of composition is not clear.

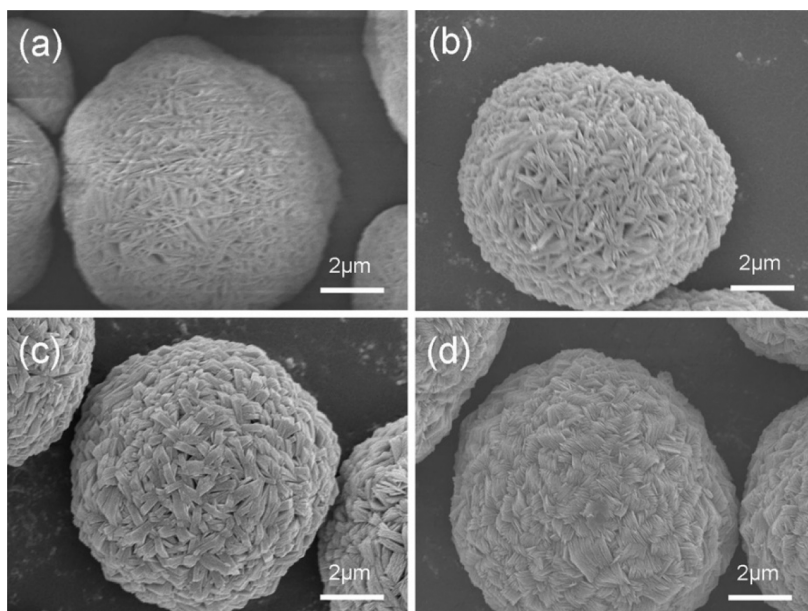
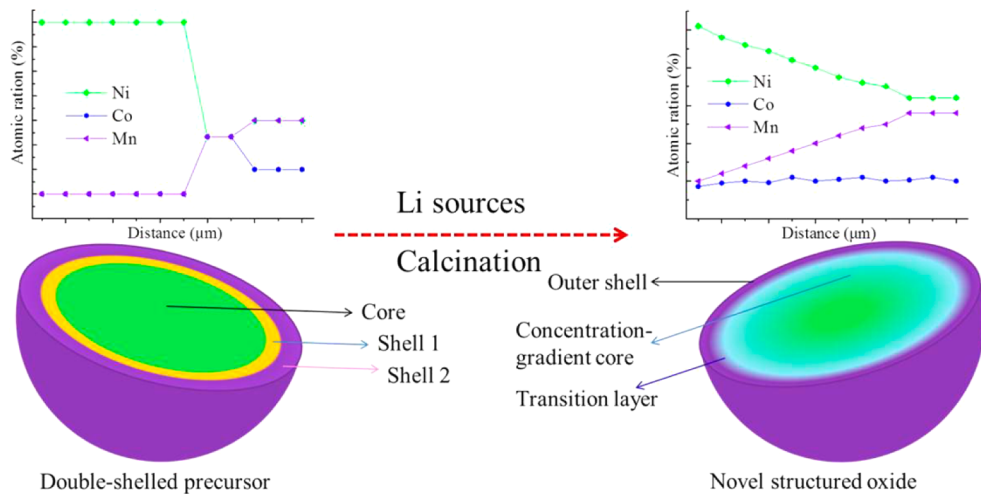
Therefore, in our previous work, we have designed the layered oxide $\text{LiNi}_{0.5}\text{Co}_{0.2}\text{Mn}_{0.3}\text{O}_2$ to double-shelled $\text{Li}[(\text{Ni}_{0.8}\text{Co}_{0.1}\text{Mn}_{0.1})_{2/7}(\text{Ni}_{1/3}\text{Co}_{1/3}\text{Mn}_{1/3})_{3/14}-(\text{Ni}_{0.4}\text{Co}_{0.2}\text{Mn}_{0.4})_{1/2}]\text{O}_2$ without compositional variation to investigate the effect of composition.^{21,22} The results demonstrate that core–shell structure indeed could enhance the electrochemical properties although compositional change affects the performance at the same time. However, follow-up studies find a structural mismatch with voids of tens of nanometers appearing between the core and shell in the prepared core–shell particles after numerous cycles, which makes the core part lose the pathway for the Li^+ ions and the electron transfer.^{23,26} Then, the concentration-gradient structure, in which the shell is replaced by a concentration-gradient outer layer, is proposed to solve the above challenge.^{23,24} As expected, durable cycle life and improved thermal stability are

Received: March 18, 2015

Accepted: May 27, 2015

Published: May 27, 2015



Scheme 1. Schematic Diagram of Double-Shelled Precursor and Novel Structured Oxide**Figure 1.** SEM images of (a) core $[\text{Ni}_{0.8}\text{Co}_{0.1}\text{Mn}_{0.1}](\text{OH})_2$, (b) one-shelled $[(\text{Ni}_{0.8}\text{Co}_{0.1}\text{Mn}_{0.1})_{4/7}(\text{Ni}_{1/3}\text{Co}_{1/3}\text{Mn}_{1/3})_{3/7}](\text{OH})_2$, (c) double-shelled $[(\text{Ni}_{0.8}\text{Co}_{0.1}\text{Mn}_{0.1})_{2/7}(\text{Ni}_{1/3}\text{Co}_{1/3}\text{Mn}_{1/3})_{3/14}(\text{Ni}_{0.4}\text{Co}_{0.2}\text{Mn}_{0.4})_{1/2}](\text{OH})_2$, and (d) normal $[\text{Ni}_{0.5}\text{Co}_{0.2}\text{Mn}_{0.3}](\text{OH})_2$.

obtained for the concentration-gradient layered oxide. Unfortunately, the origin of enhanced performance is not clear and seldom investigated until now, although core–shell and concentration-gradient layered oxide cathode materials deliver superior electrochemical properties. Understanding the origin of performances improvement in these materials is also very helpful to design new desired materials with specific properties.

In view of this, the double-shelled precursors $[(\text{Ni}_{0.8}\text{Co}_{0.1}\text{Mn}_{0.1})_{2/7}(\text{Ni}_{1/3}\text{Co}_{1/3}\text{Mn}_{1/3})_{3/14}(\text{Ni}_{0.4}\text{Co}_{0.2}\text{Mn}_{0.4})_{1/2}](\text{OH})_2$ were first prepared via a developed coprecipitation route. According to our previous study, high temperature calcination could bring partial diffusion of cation between core and shell, and the diffusion rate is highly related to concentration difference of cation between core and shell.²⁵ Therefore, diffusions of Ni, Co, and Mn cations first occur between core and inner shell in double-shelled structure during high temperature calcination. On the basis of the above result and theory, a specific structured oxide ($\text{Li}-\text{Ni}_{0.5}\text{Co}_{0.2}\text{Mn}_{0.3}\text{O}_2$), consisting of concentration-gradient core,

transition layer, and outer shell, is designed and prepared from the as-prepared double-shelled precursors in control of calcination temperature and time to illustrate the origin of performance improvement in core–shell and concentration-gradient layered oxides as high performance cathode materials for lithium-ion batteries. Schematic diagram is displayed in Scheme 1. The simple and facile method also gives a new insight into preparing specific structured materials for desired LIBs.

2. EXPERIMENTAL SECTION

2.1. Preparation of Precursors and Layered Oxides. The preparation method of double-shelled $[(\text{Ni}_{0.8}\text{Co}_{0.1}\text{Mn}_{0.1})_{2/7}(\text{Ni}_{1/3}\text{Co}_{1/3}\text{Mn}_{1/3})_{3/14}(\text{Ni}_{0.4}\text{Co}_{0.2}\text{Mn}_{0.4})_{1/2}](\text{OH})_2$ and normal $[\text{Ni}_{0.5}\text{Co}_{0.2}\text{Mn}_{0.3}](\text{OH})_2$ precursors was similar to that from our previous report.^{21,22} However, in this paper the concentration of the sulfate solution (2 M), pH (11.8 and 11.2 for core and shells respectively), the amount of chelating agent (1.5 M), and stirring speed of the mixture (600 rpm) were utilized to further optimize preparation conditions. After filtering, washing and drying, the as-

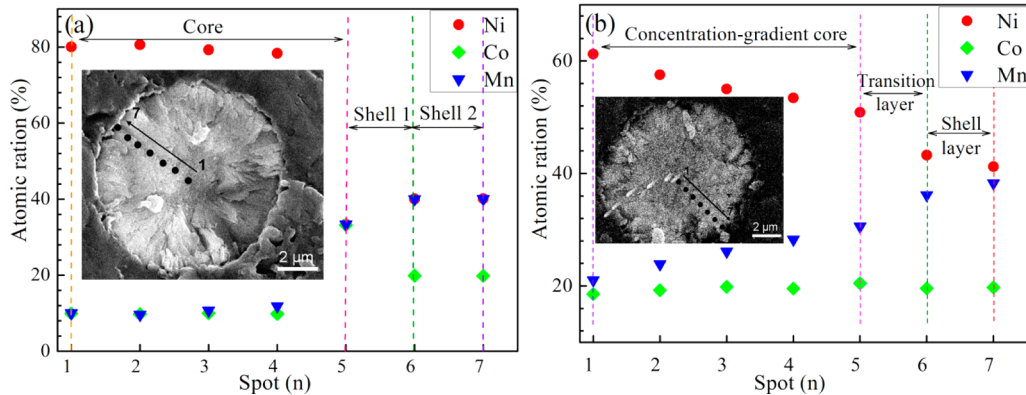


Figure 2. EDS results of Ni, Co, and Mn compositional changes on the cross-section of a single (a) double-shelled precursor and (b) layered oxide particle.

prepared precursors were calcined with stoichiometric ratio Li_2CO_3 ($\text{Li}/\text{M} = 1.05$) powders at 900°C for 2 h and then at 800°C for 10 h in a furnace under air to form the aimed layered oxides.

2.2. Materials Characterization. The particle size distribution, crystal structure, morphology, compositional changes on the cross-section of single particle, total chemical compositions of precursors, and surface state of the samples were detected by particle size analyzer (OMECA, LS-POP(6)), X-ray diffraction (XRD, Rigaku D/MAX-2500), scanning electron microscope (SEM, JMS-6700F, JEOL), energy dispersive X-ray spectroscopy (EDS, Hiroba EDX), inductively coupled plasmas spectrometer (ICP, SPS 7800, Seiko Instruments), and X-ray photoelectron spectroscopy with a monochromatic Al $\text{K}\alpha$ X-ray source (XPS, Thermo Scientific), respectively. The test conditions were similar to those from our previous work.²⁵ High resolution transmission electron microscopy (HRTEM) characterization and single-crystal selected area electron diffraction (SAED) data were conducted using a 200 kV transmission electron microscope (JEOL-JEM 2100). For HRTEM analysis, to obtain surface primary grains, the cycled electrodes were dispersed in ethanol using a sonicator. So the surface primary grains were stripped first and then transferred onto a lacey carbon-supported Cu-grid. Reitveld refinement was applied for data analysis using the WinplotR package.

For investigation of thermal stability of both delithiated oxides, cells were charged to 4.3 V (current density: 40 mA g^{-1}) and opened carefully in the Ar-filled drybox. After that, the electrode materials including active oxides and electrolyte were recovered from the Al foil. The DSC data were obtained by differential scanning calorimeter (DSC, NETZSCH 204F1) using a scan rate of 5°C min^{-1} in the range 50 – 350°C .

2.3. Electrochemical Measurements. The method of fabrication of cathode electrodes was similar to our previous report.²⁵ After drying, cathode disks of 2.0 cm^2 area were punched out, which have a similar active material loading (8.0 – 8.5 mg cm^{-2}). The cells were preliminarily charged and discharged in the potential ranges 3.0 – 4.3 , 3.0 – 4.4 , and 3.0 – 4.5 V (vs Li/Li $^+$) at 25 and 55°C . We first used a current density of 20 mA g^{-1} during the initial three cycles to fully activate the materials and then selected 100 mA g^{-1} to study the cycling stability in the subsequent cycles. A Zahner IM6ex electrochemical workstation was utilized to measure electrochemical impedance spectra (EIS) in the frequency range 100 kHz to 10 mHz .

3. RESULTS AND DISCUSSION

3.1. Material Characterization. Figure 1 shows the SEM images of core $[\text{Ni}_{0.8}\text{Co}_{0.1}\text{Mn}_{0.1}](\text{OH})_2$, one-shelled $[(\text{Ni}_{0.8}\text{Co}_{0.1}\text{Mn}_{0.1})_{4/7}(\text{Ni}_{1/3}\text{Co}_{1/3}\text{Mn}_{1/3})_{3/7}](\text{OH})_2$, double-shelled $[(\text{Ni}_{0.8}\text{Co}_{0.1}\text{Mn}_{0.1})_{2/7}-(\text{Ni}_{1/3}\text{Co}_{1/3}\text{Mn}_{1/3})_{3/14}(\text{Ni}_{0.4}\text{Co}_{0.2}\text{Mn}_{0.4})_{1/2}](\text{OH})_2$, and normal $[\text{Ni}_{0.5}\text{Co}_{0.2}\text{Mn}_{0.3}](\text{OH})_2$ precursors prepared by coprecipitation. All precursors have spherical secondary particles assembled by nanosized primary grains. Clearly, the needle-

shaped primary grains of the core and inner shell seen in Figure 1a,b change to the block-like shaped primary grains for outer shell in Figure 1c. The total chemical composition of normal and double-shelled precursors are $[\text{Ni}_{0.506}\text{Co}_{0.198}\text{Mn}_{0.296}](\text{OH})_2$ and $[\text{Ni}_{0.503}\text{Co}_{0.199}\text{Mn}_{0.298}](\text{OH})_2$ by ICP analysis. It is believed that the microsized monodisperse spherical hydroxide precursors are self-assembled on the basis of the coalescence and Ostwald-ripening mechanisms, in which small particles consume gradually in favor of larger particles to minimize surface free energy via dissolution–recrystallization.²⁷ As a result, spherical hydroxide precursors are achieved because the spherical particle has lower free energy compared with that of other morphologies.

Energy dispersive X-ray spectroscopy (EDS) is utilized to measure the compositional changes from the center toward the surface in double-shelled precursors and layered oxides. As shown in Figure 2a, Ni, Co, and Mn concentrations approach constant (about 80%, 10%, and 10% for Ni, Co, and Mn, respectively) in the range of about $4.0 \mu\text{m}$ from the core center, which corresponds to core $[\text{Ni}_{0.8}\text{Co}_{0.1}\text{Mn}_{0.1}](\text{OH})_2$. Subsequently, Ni concentration decreases sharply from about 80% to 33%, while Mn and Co concentrations increase from about 10% to 33%, which corresponds to inner shell $[\text{Ni}_{0.33}\text{Co}_{0.33}\text{Mn}_{0.33}](\text{OH})_2$. After this inner shell layer, Ni, Co, and Mn concentrations remain almost constant (about 40%, 20%, and 40% for Ni, Co and Mn, respectively), which corresponds to outer shell $[\text{Ni}_{0.4}\text{Co}_{0.2}\text{Mn}_{0.4}](\text{OH})_2$. On the basis of the EDS data, double-shelled precursors are achieved via a developed coprecipitation route.

Supporting Information Figure S1 shows the particle size distribution of core, one-shelled, and double-shelled precursors collected during coprecipitation. The average particle sizes (D_{50}) of core, one-shelled, and double-shelled precursors are 6.72 , 8.02 , and $9.96 \mu\text{m}$, respectively. These results suggest that the thicknesses of the inner shell and outer shell in double-shelled precursors are 0.65 and $0.97 \mu\text{m}$. Double-shelled precursors reveal spherical secondary particle in Figure 1c, so the morphology of double-shelled precursors can be supposed as ideal spherical particle to roughly calculate the molar ratio of core and shells. The volumes of core, inner shell, and outer shell are 37.93 , 26.55 , and $59.03 \mu\text{m}^{-3}$, respectively. Thus, the molar ratio of the core, inner shell, and outer shell in as-prepared double-shelled precursors is $0.307/0.215/0.478$, considering the densities and formula weights of the core, inner shell, and outer shell are almost similar. The value can align well with the aimed one ($0.286/0.214/0.5$).

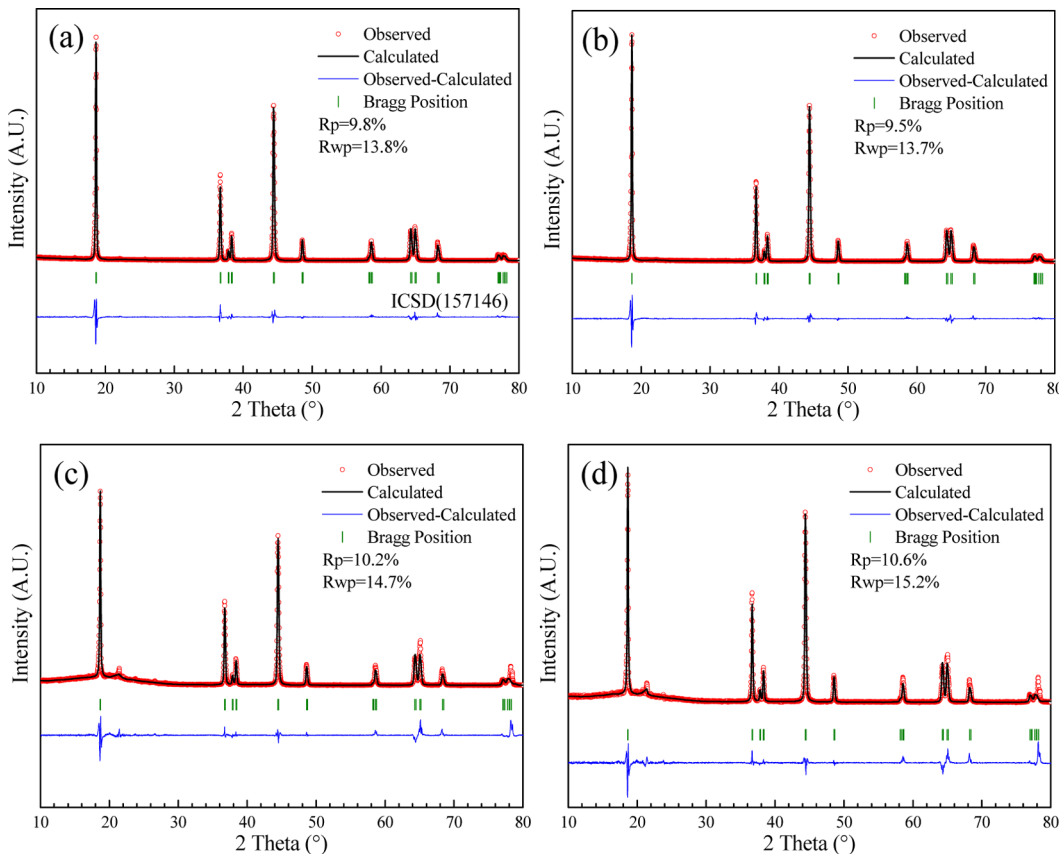


Figure 3. Rietveld refinement of powder X-ray diffraction for (a) pristine NL-LNCM, (b) SSL-LNCM, and cycled (c) NL-LNCM, and (d) SSL-LNCM electrodes in the discharged state after 110 cycles in the range 3.0–4.4 V at 55 °C.

After lithiation, the compositional variation of Ni, Co, and Mn concentrations are detected from center to surface of a single particle, which is shown in Figure 2b. From center to spot 5 along the cross section of the particle, Ni concentration decreases gradually, and Mn concentration increases continuously, whereas Co concentration remains constant at about 20% (which is much different from that of double-shelled precursors in Figure 2a), leading to a concentration-gradient core. From spot 5 to spot 6, a transition layer is detected. After the transition layer, the Ni, Co, and Mn concentrations approximately keep constant (about 42%, 20%, and 38%, respectively) to form an outer shell of about 1.0 μm . The EDS results of line scan on the cross-section of single particle are revealed in Supporting Information Figure S2. Those maps of Ni K_α1, Co K_α1, and Mn K_α1 in Supporting Information Figure S2b indicate the distributions of Ni, Co, and Mn are in line with the designed structure. It is clear that Ni concentration decreases gradually from the midpoint out toward the surface (about from 5 to 1.5 μm and 5 to 8.5 μm in EDS line) in Supporting Information Figure 2Sc, whereas the higher Mn concentration is found in the outer layer (about from 0.5 to 1.5 μm and 8.5 to 9.5 μm in EDS line) in Supporting Information Figure 2Sd. As for Co concentration, it remains almost constant in total line in Supporting Information Figure 2Se. Therefore, on the basis of the above EDS data, the specific structured layered $\text{LiNi}_{0.5}\text{Co}_{0.2}\text{Mn}_{0.3}\text{O}_2$ (SSL-LNCM), which consists of concentration-gradient core, transition layer, and outer shell, is successfully achieved from double-shelled precursors.

Figure 3a shows refined XRD patterns of pristine normal and specific structured layered oxides. Both oxides could be indexed

to a well-defined hexagonal $\alpha\text{-NaFeO}_2$ -type structure with a space group of $R\bar{3}m$.²⁷ Furthermore, the clear split between the adjacent peaks of (006)/(102) and (018)/(110) suggests a typical layered structure for both materials.^{27,28} The refined lattice parameters of both pristine layered oxides are listed in Table 1. Normal layered $\text{LiNi}_{0.5}\text{Co}_{0.2}\text{Mn}_{0.3}\text{O}_2$ (NL-LNCM) and

Table 1. Refined Lattice Parameters of Pristine Normal and Specific Structured Layered Oxides as Well as the Cycled Electrodes

sample	lattice params		
	<i>a</i> -axis/ \AA	<i>c</i> -axis/ \AA	<i>V</i> / \AA^3
pristine NL-LNCM	2.8678	14.237	101.404
pristine SSL-LNCM	2.8672	14.232	101.321
cycled NL-LNCM	2.8657	14.247	101.328
cycled SSL-LNCM	2.8677	14.252	101.499

SSL-LNCM exhibit almost the same lattice parameters, *a* values and *c* values. SEM images of NL-LNCM and SSL-LNCM are shown in Supporting Information Figure S3, and both of them still display spherical morphology. There is no obvious disruption of the particle morphology for specific structured layered oxide in Supporting Information Figure S3b, which is usually caused by the different shrinkage ratio of two different hydroxide compositions during the calcination process.²⁶ Also, the block-like shaped primary grains of precursors in Figure 1c,d change into a plate-like shape after being calcined, as in Supporting Information Figure S3a,b.

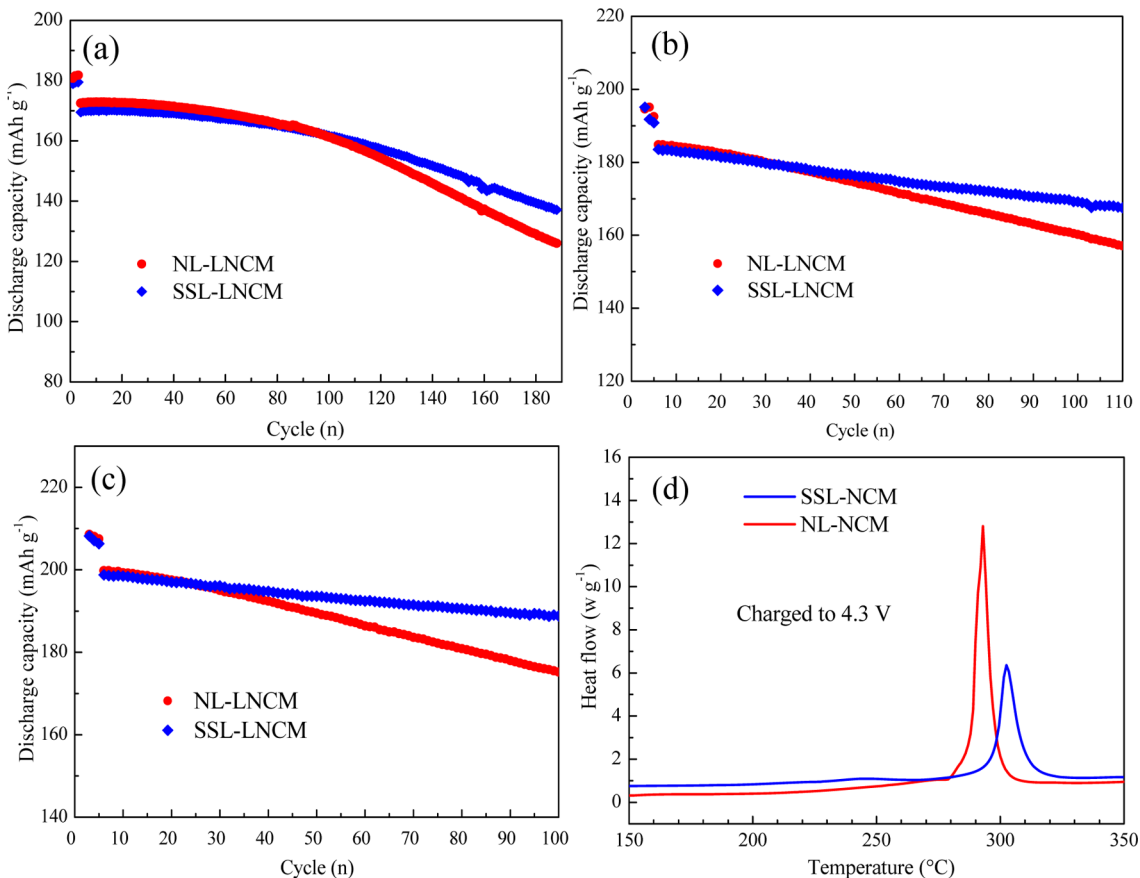


Figure 4. Cycle performance of NL- and SSL-LNCM in the ranges (a) 3.0–4.3 V, (b) 3.0–4.4 V, and (c) 3.0–4.5 V at 55 °C, and (d) DSC results of both layered oxide electrodes charged to 4.3 V.

3.2. Electrochemical Properties and Thermal and Structural Stability.

At the current time, in the commercialized Li-ion battery the layered compounds are usually charged to 4.3 V (vs Li/Li⁺). To enhance battery energy density, researchers are struggling to elevate charge up-voltage to 4.4 or 4.5 V to utilize the remained Li⁺ in the layered structured compounds. However, as mentioned in the Introduction, the common layered compounds such as LiNi_{0.5}Co_{0.2}Mn_{0.3}O₂ will suffer from structural instability, deteriorated cyclability, and worsened thermal stability as they are charged up to 4.3 V. Core–shell structure may function to resolve this problem. In this work, the synthesized compounds are subject to charge–discharge tests in the potential ranges of 4.3, 4.4, and 4.5 V. The initial charge–discharge curves of NL- and SSL-LNCM are revealed in Supporting Information Figure S4. The SSL-LNCM electrode delivers large specific capacities of 172.7, 184.5, and 203.5 mAh g⁻¹ in the potential ranges 3.0–4.3, 3.0–4.4, and 3.0–4.5 V, respectively, which are similar to those of NL-LNCM. Nevertheless, the specific structured layered oxide electrodes exhibit improved Li⁺ intercalation stability as expected in Figure 4 and Supporting Information Figure S5. As revealed in Supporting Information Figure S5a, in the range 3.0–4.3 V at 25 °C, the specific structured layered oxide electrode has a capacity retention of 86.45% (134.1 mAh g⁻¹) after 220 cycles, but the normal layered oxide electrode suffers from a severe capacity fading, leading to a capacity retention of only 73.57% (115.5 mAh g⁻¹) over the same cycles. To further evaluate the cycling stability of the specific structured layered oxide electrode, testing temperature is improved to 55 °C in

Figure 4a. SSL-LNCM electrode displays more excellent cycle performance because of complete encapsulation with a stable outer shell, and maintains a reversible capacity of 142.2 mAh g⁻¹ (capacity loss only 12.60%) after 190 cycles. By contrast, NL-LNCM electrode shows a rapid decrease in capacity, leading to capacity retention of only 73.04% (126.1 mAh g⁻¹). Meanwhile, from Figure 4b and Supporting Information Figure S5b with the improved up-voltage to 4.4 V, SSL-LNCM electrode still reveals the superior capacity retentions of 89.76% (at 25 °C after 150 cycles) and 91.28% (at 55 °C after 110 cycles), compared with 80.54% and 84.95% of the NL-LNCM electrode. As charged to 4.5 V in Figure 4c, the SSL-LNCM electrode has capacity retention of 188.8 mAh g⁻¹ after 100 cycles, while the NL-LNCM electrode suffers from a severe capacity fading, leading to an inferior capacity of only 175.2 mAh g⁻¹ over the same cycles. In a comparison with the reported LiNi_{0.5}Co_{0.2}Mn_{0.3}O₂ in refs 21, 22, 29, and 30, the SSL-LNCM electrode in this work also exhibits much improved cycling performance.

The thermal stability of cathode materials plays a very important role in cell safety, especially for the large cells in PHEVs and EVs.³¹ DSC profiles of NL- and SSL-LNCM electrodes charged to 4.3 V are revealed in Figure 4d. NL- and SSL-LNCM show different tendencies of heat generation. A large exothermic peak in the NL-LNCM electrode appears at 290.2 °C with heat generation of 972.6 J g⁻¹. In contrast, the exothermic peak in the SSL-LNCM electrode appears at 302.1 °C with low heat generation of 609.9 J g⁻¹. As a result, a highly

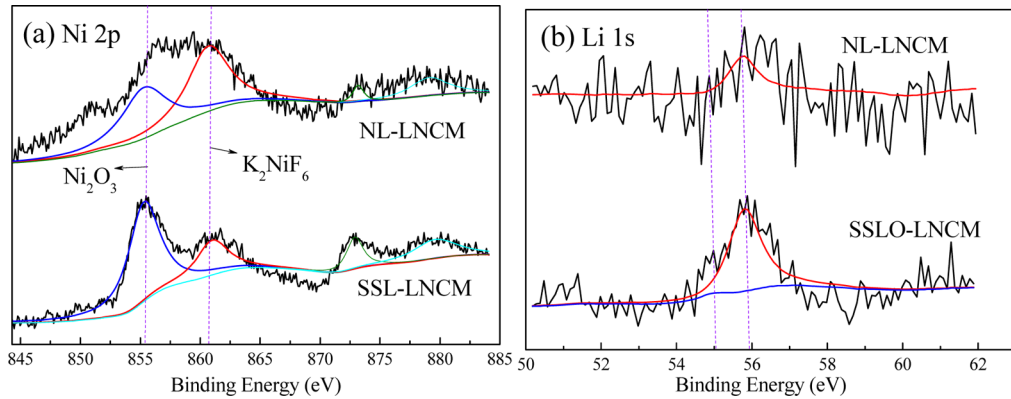


Figure 5. XPS spectra of NL- and SSL-LNCM after 110 cycles in the range 3.0–4.4 V at 55 °C: (a) Ni 2p spectrum and (b) Li 1s spectrum.

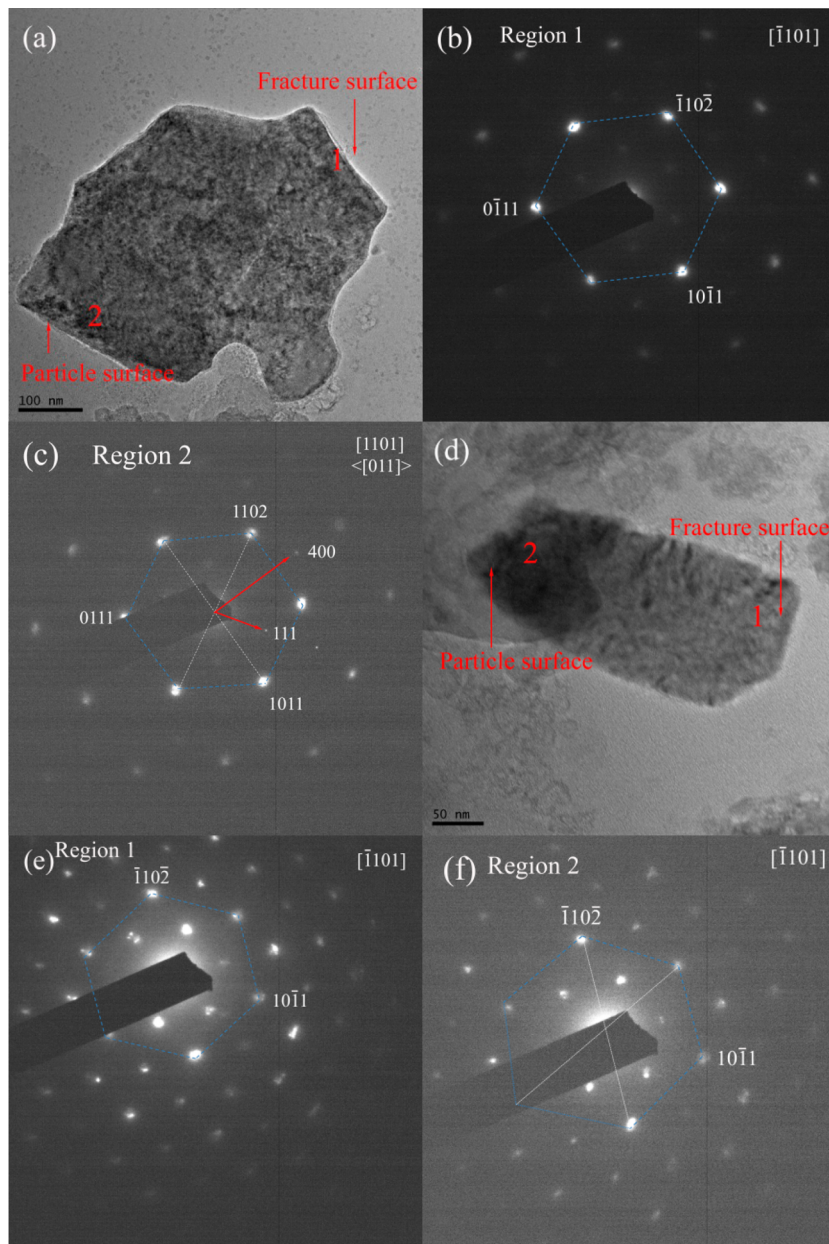


Figure 6. TEM images of (a) NL- and (d) SSL-LNCM surface primary grains; (b and c) SAED patterns of NL-LNCM at the regions marked in part a; (e and f) SAED patterns of SSL-LNCM at the regions marked in part d.

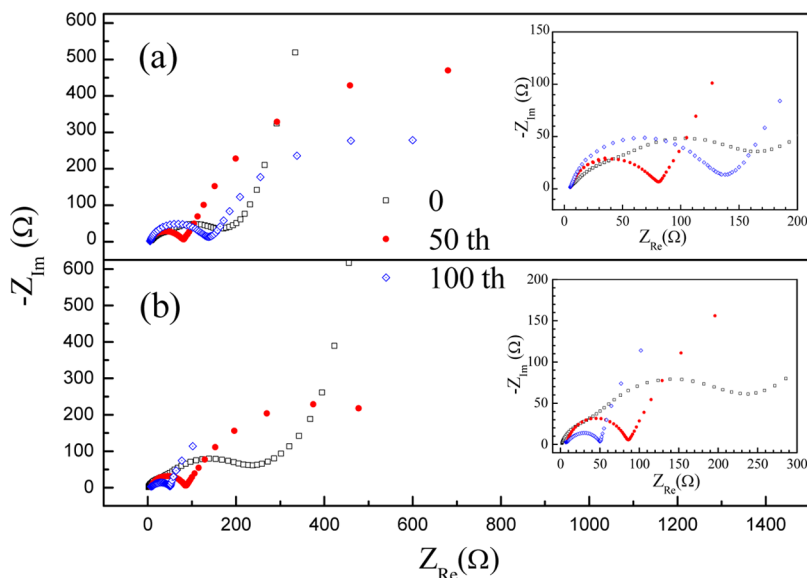


Figure 7. Impedance spectra of the (a) NL- and (b) SSL-LNCM electrodes in the discharged state at different cycles.

delithiated SSL-LNCM electrode might display excellent safety properties in a lithium-ion battery system.

For an investigation of structural stability during cycling, XRD data on the discharged electrodes cycled to the 110th cycle in the range 3.0–4.4 V at 55 °C are collected and refined as shown in Figure 3c,d. The single phase of layered structure with $R\bar{3}m$ is maintained throughout cycling for both NL- and SSL-LNCM electrodes. From the refined lattice parameters shown in Table 1, the *a*-axis spacing slightly decreases for NL-LNCM compared with that of a pristine sample, while the *a*-axis spacing of cycled SSL-LNCM electrode is almost identical to that of SSL-LNCM before cycling. Interestingly, the *c*-axis spacing of both electrodes increases mildly.

3.3. Origin of Improved Performances for SSL-LNCM.

As to these core–shell and concentration-gradient materials, the origin of enhanced properties is not completely clear at current and is seldom investigated. Understanding the origin is much helpful to design new desired materials with specific properties. From the bulk structural change during cycling as investigated above, the plausible origin is not found. Hence, in this section, the structural transformation of cycled particle surface is studied in detail via XPS, TEM, and EIS to reveal the underlying reasons of the improved performances for SSL-LNCM. The XPS spectra of NL- and SSL-LNCM after 110 cycles in the range 3.0–4.4 V (vs Li/Li⁺) at 55 °C are displayed in Figure 5 and Supporting Information Figure S6. From Figure 5a, the Ni 2p_{3/2} binding energies of both cycled materials are about 855 and 861 eV, which are in accordance with standard Ni³⁺ (855.1 eV)³² and Ni⁴⁺ (860.9 eV).³³ Obviously, an unobtrusive energy shift of Ni 2p_{3/2} to a higher oxidation state could be identified, especially for NL-LNCM. A similar phenomenon is also reported in previous research.³³ In addition, the valence state of Ni element tends to a higher state of ⁴⁺ for NL-LNCM. As can be seen in Supporting Information Figure S6a, the Co 2p_{3/2} spectrum of NL-LNCM after cycles shows a Co⁴⁺ major peak at 781.9 eV comparable with that of Co³⁺ (779.6 eV) in LiCoO₂.^{32,34,35} However, the valence state of Co mainly maintains +3 in a fully discharged state for SSL-LNCM. The Mn 2p_{3/2} spectrum in Supporting Information Figure S6b shows that both Mn³⁺ and Mn⁴⁺ coexist, because two major peaks with binding energies of

641.6 and 642.7 eV are observed, which are close to the values of Mn³⁺ in Mn₂O₃, and Mn⁴⁺ in LiNi_{0.5}Mn_{0.5}O₂ and MnO₂.^{36–38} Interestingly, the intensity of the Li 1s spectrum in NL-LNCM is very weak compared with that in SSL-LNCM, meaning low Li content on the particle surface of cycled NL-LNCM.

The bulk and surface changes of NL- and SSL-LNCM are characterized by transmission electron microscopy (TEM) and selected area electron diffraction (SAED) to further explore the origin of improved properties. The fracture marked in Figure 6 has a pointed edge, which is attributed to the breakage of primary grains during the ultrasonic process. By contrast, the other surfaces show a smooth edge. Thus, we can determine the fracture surface in primary grains. The TEM images and single-crystal SAED patterns collected from different regions are shown in Figure 6. Figure 6b,e,f only shows 6-fold symmetry (highlighted by a dashed hexagon), which is the SAED pattern along the [1101] zone axis (indexed based on hexagonal structure) for the $R\bar{3}m$ space group.³⁹ However, a spinel phase (LiNi_xCo_yMn_{2-x-y}O₄) is observed on the particle surface of cycled NL-LNCM except for the layered phase in Figure 6c, which is in accordance with the weaker intensity of the Li spectrum in Figure 5d because the spinel phase has a lower Li content than the layered phase. Besides, the valence states of transition metal in spinel phase are higher than those of the layered phase, which is also in accordance with XPS results (a more obvious energy shift of Ni 2p_{3/2} to a higher oxidation state is observed for NL-LNCM).

Electrochemical impedance spectroscopy (EIS) is used to understand the beneficial effect of the outer layer (shell) on the improved performances of the SSL-LNCM samples. Figure 7 presents Nyquist plots measured before and after different cycles. The semicircle in the high frequency region is related to surface film resistance and the charge-transfer process, and the straight line and arc-like profile in the low frequency region are attributed to a semi-infinite Warburg diffusion process in the bulk and a finite Nernst diffusion process in a thin layer, respectively.^{27,40} The simulated electrochemical parameters are shown in Table 2 using the equivalent circuit in Supporting Information Figure S7. As expected, after 110 cycles in the range 3.0–4.4 V at 55 °C, the surface film resistance R_{sf} and

Table 2. Simulated Results from Electrochemical Impedance Spectra of NL- and SSL-LNCM after Different Cycles in the Range 3.0–4.4 V at 55 °C

sample	cycle	$R_{sf} + R_{ct}$ (Ω)	W_s (Ω)	W_o (Ω)
NL-LNCM	0	160.8		138.4
	50th	71.0	387.4	6.1
	100th	117.9	286.1	37.9
SSL-LNCM	0	192.2		423.2
	50th	75.8	254.5	3.0
	100th	41.5	9.5	8.1

charge-transfer resistance R_{ct} of SSL-LNCM are much smaller than that of NL-LNCM.

On the basis of the above results, we believe that the particle surface (shell layer) plays an important role in achieving superior electrochemical properties for the layered oxide materials. First, the shell layer prevents the sensitively active cores from directly contacting the electrolyte, avoiding or restricting the loss of active compositions. Second, the stable shell layer presumably can work as an HF scavenger to react with HF released from electrolytes prior to active cores.⁴¹ As a result, after numerous cycles for NL-LNCM, the deficient spinel/layered mixed phase on particle surface occurs, which causes high surface film resistance and charge-transfer resistance. Consequentially, the NL-LNCM electrode exhibits inferior properties, especially at high operating voltage and temperature. By contrast, the SSL-LNCM maintains a pure layered phase over the same condition, and superior cycle stability is achieved.

4. CONCLUSIONS

Double-shelled $[(\text{Ni}_{0.8}\text{Co}_{0.1}\text{Mn}_{0.1})_{2/7}(\text{Ni}_{1/3}\text{Co}_{1/3}\text{Mn}_{1/3})_{3/14} \cdot (\text{Ni}_{0.4}\text{Co}_{0.2}\text{Mn}_{0.4})_{1/2}](\text{OH})_2$ precursors are first prepared via a developed coprecipitation route. After being calcined with lithium carbonate by controlling temperature and time, a specific structured layered oxide ($\text{LiNi}_{0.5}\text{Co}_{0.2}\text{Mn}_{0.3}\text{O}_2$) consisting of a concentration-gradient core, transition layer, and outer shell, is achieved from the as-prepared double-shelled precursors. As expected, the SSL-LNCM displays outstanding cycle life and thermal stability. After 110 cycles in the range 3.0–4.4 V at 55 °C, the valence state of Ni and Co at a normal layered oxide surface tends to a higher oxidation state than that of the specific structured oxide after numerous cycles. This can be supported by TEM, SAED, and EIS results that show that the spinel phase is observed on the particle surface except for the layered structure for the normal sample, and then the deficient spinel/layered mixed phases lead to high surface film and charge-transfer resistance, whereas the specifically structured one still remains the layered structure. Those results first illustrate the possible origin of improved electrochemical performance of layered core–shell and concentration-gradient cathode materials from surface or interface electrochemistry/structure. It will provide new insights into preparing the desired cathode materials for the next generation LIBs.

ASSOCIATED CONTENT

Supporting Information

Particle size distribution, linear scanning EDS results, SEM images, the initial charge–discharge curves, cycle life performance of NL-LNCM and SSL-LNCM at 25 °C, XPS spectra, and equivalent circuits. The Supporting Information is available free

of charge on the ACS Publications website at DOI: 10.1021/acsami.5b02373.

AUTHOR INFORMATION

Corresponding Author

*E-mail: tianjinzhanglei@163.com.

Present Address

[§]Institute of New Energy Material Chemistry, Collaborative Innovation Center of Chemical Science and Engineering (Tianjin), Tianjin Key Laboratory of Metal and Molecule Based Material Chemistry, Nankai University, Tianjin 300071, China.

Author Contributions

[†]D. Song and P. Hou contributed equally to this work.

Notes

The authors declare no competing financial interest.

ACKNOWLEDGMENTS

This work was financially supported partly by National 863 Program of China (2013AA050906), NSFC (51272175, 21301127), and Natural Science Foundation of Tianjin (15JCQNJC06400).

REFERENCES

- (1) Tarascon, J. M.; Armand, M. Issues and Challenges Facing Rechargeable Lithium Batteries. *Nature* **2001**, *414*, 359–367.
- (2) Simon, P.; Gogotsi, Y.; Dunn, B. Where Do Batteries End and Supercapacitors Begin? *Science* **2014**, *343*, 1210–1211.
- (3) Lu, Z.; MacNeil, D. D.; Dahn, J. R. Layered $\text{Li}[\text{Ni}_x\text{Co}_{1-2x}\text{Mn}_x]\text{O}_2$ Cathode Materials for Lithium-Ion Batteries. *Electrochim. Solid-State Lett.* **2001**, *4*, A200–A203.
- (4) MacNeil, D.; Lu, Z.; Dahn, J. R. Structure and Electrochemistry of $\text{Li}[\text{Ni}_x\text{Co}_{1-2x}\text{Mn}_x]\text{O}_2$ ($0 \leq x \leq 1/2$). *J. Electrochim. Soc.* **2002**, *149*, A1332–A1336.
- (5) Kalluri, S.; Pang, W. K.; Seng, K. H.; Chen, Z. X.; Guo, Z. P.; Liu, H. K.; Dou, S. X. One-Dimensional Nanostructured Design of $\text{Li}_{1+x}(\text{Mn}_{1/3}\text{Ni}_{1/3}\text{Fe}_{1/3})\text{O}_2$ as a Dual Cathode for Lithium-Ion and Sodium-Ion Batteries. *J. Mater. Chem. A* **2015**, *1*, 250–257.
- (6) Jouanneau, S.; Macneil, D. D.; Lu, Z.; Beattie, S. D.; Murphy, G.; Dahn, J. R. Morphology and Safety of $\text{Li}[\text{Ni}_x\text{Co}_{1-2x}\text{Mn}_x]\text{O}_2$ ($0 \leq x \leq 1/2$). *J. Electrochim. Soc.* **2003**, *150*, A1299–A1304.
- (7) Zhang, C. J.; He, X.; Kong, Q. S.; Li, H.; Hu, H.; Wang, H. B.; Gu, L.; Wang, L.; Cui, G. L.; Chen, L. Q. A Novel Assembly of LiFePO_4 Microspheres from Nanoplates. *CrystEngComm* **2012**, *14*, 4344–4349.
- (8) Ohzuku, T.; Makimura, Y. Layered Lithium Insertion Material of $\text{LiCo}_{1/3}\text{Ni}_{1/3}\text{Mn}_{1/3}\text{O}_2$ for Lithium-Ion Batteries. *Chem. Lett.* **2001**, *7*, 642–643.
- (9) Ngala, J. K.; Chernova, N. A.; Whittingham, M. S.; Mamak, M.; Zavalij, P. Y.; Whittingham, M. S. The Synthesis, Characterization and Electrochemical Behavior of the Layered $\text{LiNi}_{0.4}\text{Mn}_{0.4}\text{Co}_{0.2}\text{O}_2$ Compound. *J. Mater. Chem.* **2004**, *14*, 214–220.
- (10) Zhang, C. J.; Gu, L.; Kaskhedikar, N.; Cui, G. L.; Maier, J. Preparation of Silicon@Silicon Oxide Core-Shell Nanowires from a Silica Precursor toward a High Energy Density Li-Ion Battery Anode. *ACS Appl. Mater. Interfaces* **2013**, *5*, 12340–12345.
- (11) Kang, S. H.; Kim, J.; Stoll, M. E.; Sun, Y. K.; Amine, K. Layered $\text{Li}(\text{Ni}_{0.5-x}\text{Mn}_{0.5-x}\text{M}_{2x'})\text{O}_2$ ($M' = \text{Co}, \text{Al}, \text{Ti}; x = 0, 0.025$) Cathode Materials for Li-ion Rechargeable Batteries. *J. Power Sources* **2002**, *112*, 41–48.
- (12) Choi, J.; Manthiram, A. Structural and Electrochemical Characterization of the Layered $\text{LiNi}_{0.5-y}\text{Mn}_{0.5-y}\text{Co}_{2y}\text{O}_2$ ($0 \leq 2y \leq 1$) Cathodes. *Solid State Ionics* **2005**, *176*, 2251–2256.
- (13) Rao, C. V.; Reddy, A. L. M.; Ishikawa, Y.; Ajayan, P. M. $\text{LiNi}_{1/3}\text{Co}_{1/3}\text{Mn}_{1/3}\text{O}_2$ -Graphene Composite as a Promising Cathode

- for Lithium-Ion Batteries. *ACS Appl. Mater. Interfaces* **2011**, *3*, 2966–2972.
- (14) Li, J. L.; Yao, R. M.; Cao, C. B. LiNi_{1/3}Co_{1/3}Mn_{1/3}O₂ Nanoplates with {010} Active Planes Exposing Prepared in Polyol Medium as a High Performance Cathode for Li-Ion Battery. *ACS Appl. Mater. Interfaces* **2014**, *6*, 5075–5082.
- (15) Sun, Y. K.; Lee, D. J.; Lee, Y. J.; Chen, Z. H.; Myung, S. T. Cobalt-Free Nickel Rich Layered Oxide Cathodes for Lithium-Ion Batteries. *ACS Appl. Mater. Interfaces* **2013**, *5*, 11434–11440.
- (16) Li, D.; Sasaki, Y.; Kageyama, M.; Kobayakawa, K.; Sato, Y. Structure, Morphology and Electrochemical Properties of Li-Ni_{0.5}Mn_{0.5-x}Co_xO₂ Prepared by Solid State Reaction. *J. Power Sources* **2005**, *148*, 85–89.
- (17) Cho, Y. H.; Jang, D.; Yoon, J.; Kim, H.; Ahn, T. K.; Nam, K. W.; Sung, Y. E.; Kim, W. S.; Lee, Y. S.; Yang, X. Q.; Yoon, W. S. Thermal Stability of Charged LiNi_{0.5}Co_{0.2}Mn_{0.3}O₂ Cathode for Li-Ion Batteries Investigated by Synchrotron Based in Situ X-ray Diffraction. *J. Alloys Compd.* **2013**, *S62*, 219–223.
- (18) Yang, X.; Wang, X.; Hu, L.; Zou, G.; Su, S.; Bai, Y.; Shu, H.; Wei, Q.; Hu, B.; Ge, L.; Wang, D.; Liu, L. Layered Li[Ni_{0.5}Co_{0.2}Mn_{0.3}]₂-Li₂MnO₃ Core–Shell Structured Cathode Material with Excellent Stability. *J. Power Sources* **2013**, *242*, 589–596.
- (19) Sun, Y. K.; Myung, S. T.; Kim, M. H.; Prakash, J.; Amine, K. Synthesis and Characterization of Li-[Ni_{0.8}Co_{0.1}Mn_{0.1}]_{0.8}(Ni_{0.5}Mn_{0.5})_{0.2}]O₂ with the Microscale Core–Shell Structure as the Positive Electrode Material for Lithium Batteries. *J. Am. Chem. Soc.* **2005**, *127*, 13411–13418.
- (20) Lee, K. S.; Myung, S. T.; Sun, Y. K. Synthesis and Electrochemical Performances of Core–Shell structured Li-[Ni_{1/3}Co_{1/3}Mn_{1/3}]_{0.8}(Ni_{1/2}Mn_{1/2})_{0.2}]O₂ Cathode Material for Lithium Ion Batteries. *J. Power Sources* **2010**, *195*, 6043–6048.
- (21) Hou, P. Y.; Guo, J.; Song, D. W.; Zhang, J.; Zhou, E. L.; Zhang, L. Q. A Novel Double-Shelled LiNi_{0.5}Co_{0.2}Mn_{0.3}O₂ Cathode Material for Li-Ion Batteries. *Chem. Lett.* **2012**, *41*, 1712–1714.
- (22) Hou, P. Y.; Wang, X. Q.; Song, D. W.; Shi, X. X.; Zhang, L. Q.; Guo, J.; Zhang, J. Design, Synthesis, and Performances of Double-Shelled LiNi_{0.5}Co_{0.2}Mn_{0.3}O₂ as Cathode for Long-Life and Safe Li-Ion Battery. *J. Power Sources* **2014**, *265*, 174–181.
- (23) Sun, Y. K.; Myung, S. T.; Park, B. C.; Prakash, J.; Belharouak, I.; Amine, K. High-Energy Cathode Material for Long-Life and Safe Lithium Batteries. *Nat. Mater.* **2009**, *8*, 320–324.
- (24) Sun, Y. K.; Chen, Z. H.; Noh, H. J.; Lee, D. J.; Jung, H. G.; Ren, Y.; Wang, S.; Yoon, C. S.; Myung, S. T.; Amine, K. Nanostructured High-Energy Cathode Materials for Advanced Lithium Batteries. *Nat. Mater.* **2012**, *11*, 942–947.
- (25) Hou, P. Y.; Wang, X. Q.; Guo, J.; Zhang, J.; Song, D. W.; Shi, X. X.; Wang, D. G.; Zhang, L. Q. A Novel Core–Concentration Gradient-Shelled LiNi_{0.5}Co_{0.2}Mn_{0.3}O₂ as High-Performance Cathode for Lithium-Ion Batteries. *RSC Adv.* **2014**, *4*, 15923–15929.
- (26) Sun, Y. K.; Myung, S. T.; Park, B. C.; Amine, K. Synthesis of Spherical Nano- to Microscale Core–Shell Particles Li-[Ni_{0.8}Co_{0.1}Mn_{0.1}]_{1-x}(Ni_{0.5}Mn_{0.5})_x]O₂ and Their Applications to Lithium Batteries. *Chem. Mater.* **2006**, *18*, 5159–5163.
- (27) Hou, P. Y.; Zhang, L. Q.; Gao, X. P. A High-Energy, Full Concentration-Gradient Cathode Material with Excellent Cycle and Thermal Stability for Lithium Ion Batteries. *J. Mater. Chem. A* **2014**, *2*, 17130–17138.
- (28) Meng, Y. S.; Ceder, G.; Grey, C. P.; Yoon, W. S.; Yang, S. H. Understanding the Crystal Structure of Layered LiNi_{0.5}Mn_{0.5}O₂ by Electron Diffraction and Powder Diffraction Simulation. *Electrochem. Solid-State Lett.* **2004**, *7*, A155–A158.
- (29) Liu, X. H.; Kou, L. Q.; Shi, T.; Liu, K.; Chen, L. Excellent high rate capability and high voltage cycling stability of Y₂O₃-coated LiNi_{0.5}Co_{0.2}Mn_{0.3}O₂. *J. Power Sources* **2014**, *267*, 874–880.
- (30) Xia, L.; Qiu, K. H.; Gao, Y. Y.; He, X.; Zhou, F. D. High Potential Performance of Cerium-Doped LiNi_{0.5}Co_{0.2}Mn_{0.3}O₂ Cathode Material for Li-Ion Battery. *J. Mater. Sci.* **2015**, *50*, 2914–2920.
- (31) Sun, Y. K.; Kima, D. H.; Junga, H. G.; Myungc, S. T.; Amine, K. High-Voltage Performance of Concentration-Gradient Li-[Ni_{0.67}Co_{0.15}Mn_{0.18}]O₂ Cathode Material for Lithium-Ion Batteries. *Electrochim. Acta* **2010**, *55*, 8621–8627.
- (32) Moses, A. W.; Garcia Flores, H. G.; Kim, J. G.; Langell, M. A. Surface Properties of LiCoO₂, LiNiO₂ and LiNi_{1-x}Co_xO₂. *Appl. Surf. Sci.* **2007**, *253*, 4782–4788.
- (33) Lin, F.; Nordlund, D.; Markus, I. M.; Weng, T. C.; Xin, H. L.; Doeff, M. M. Profiling the Nanoscale Gradient in Stoichiometric Layered Cathode Particles for Lithium-Ion Batteries. *Energy Environ. Sci.* **2014**, *7*, 3077–3085.
- (34) Dupin, J. C.; Gonbeau, D.; Benqlilou-Moudden, H.; Vinatier, P.; Levasseur, A. XPS Analysis of New Lithium Cobalt Oxide Thin-Films before and after Lithium Deintercalation. *Thin Solid Films* **2001**, *384*, 23–32.
- (35) Cherkashinin, G.; Ensling, D.; Jaegermann, W. LiMO₂ (M = Ni, Co) Thin Film Cathode Materials: A Correlation between the Valence State of Transition Metals and the Electrochemical Properties. *J. Mater. Chem. A* **2014**, *2*, 3571–3580.
- (36) Chen, Y.; Xu, G.; Li, J.; Zhang, Y.; Chen, Z.; Kang, F. High Capacity 0.5Li₂MnO₃·0.5LiNi_{0.33}Co_{0.33}Mn_{0.33}O₂ Cathode Material via a Fast Co-Precipitation Method. *Electrochim. Acta* **2013**, *87*, 686–692.
- (37) Qiao, Q. Q.; Zhang, H. Z.; Li, G. R.; Ye, S. H.; Wang, C. W.; Gao, X. P. Surface Modification of Li-Rich Layered Li-(Li_{0.17}Ni_{0.25}Mn_{0.58})O₂ Oxide with Li-Mn-PO₄ as the Cathode for Lithium-Ion Batteries. *J. Mater. Chem. A* **2013**, *1*, 5262–5268.
- (38) Yu, Z. N.; Duong, B.; Abbott, D.; Thomas, J. Highly Ordered MnO₂ Nanopillars for Enhanced Supercapacitor Performance. *Adv. Mater.* **2013**, *25*, 3302–3306.
- (39) Wang, D.; Belharouak, I.; Zhou, G.; Amine, K. Nanoarchitecture Multi-Structural Cathode Materials for High Capacity Lithium Batteries. *Adv. Funct. Mater.* **2013**, *23*, 1070–1075.
- (40) Kuang, F.; Zhang, D.; Li, Y. J.; Wan, Y.; Hou, B. R. Electrochemical Impedance Spectroscopy Analysis for Oxygen Reduction Reaction in 3.5% NaCl Solution. *J. Solid State Electrochem.* **2009**, *13*, 385–390.
- (41) Su, L.; Jing, Y.; Zhou, Z. Li Ion Battery Materials with Core–Shell Nanostructures. *Nanoscale* **2011**, *3*, 3967–3983.